

Accessing the diffracted wavefield by coherent subtraction

Benjamin Schwarz¹ and Dirk Gajewski²

¹*Department of Earth Sciences, University of Oxford, South Parks Road, Oxford OX1 3AN, United Kingdom*

²*Institute of Geophysics, University of Hamburg, Bundesstr. 55, 20146 Hamburg, Germany*

6 July 2017

SUMMARY

Diffractions have unique properties which are still rarely exploited in common practice. Aside from containing sub-wavelength information on the scattering geometry or indicating small-scale structural complexity, they provide superior illumination compared to reflections. While diffraction occurs arguably on all scales and in most realistic media, the respective signatures typically have low amplitudes and are likely to be masked by more prominent wavefield components. It has been widely observed that automated stacking acts as a directional filter favoring the most coherent arrivals. In contrast to other works, which commonly aim at steering the summation operator towards fainter contributions, we utilize this directional selection to coherently approximate the most dominant arrivals and subtract them from the data. Supported by additional filter functions which can be derived from wavefront attributes gained during the stacking procedure, this strategy allows for a fully data-driven recovery of the faint diffracted background wavefield and makes it accessible for further processing. Large source-receiver offset acquisition offers the benefits of high data redundancy and improved illumination. However, large-offset recordings are generally expensive to acquire and the majority of academic research is confronted with a comparably low channel count and target depths that significantly exceed the available offset range. A complex single-channel field data example recorded in the Aegean sea near Santorini illustrates that the diffracted background wavefield is surprisingly

rich and despite the absence of a high channel count can still be detected and characterized, suggesting a variety of applications in industry and academia.

Key words: Diffraction; Coherence; Stacking; Illumination; Seismology; GPR

1 INTRODUCTION

In hydrocarbon exploration, multi-channel seismic is a standard tool to infer the Earth's structure on the reservoir scale. Despite the benefits of increased illumination, massive multi-channel acquisitions are generally challenging and in most cases not affordable for small companies or academic institutions. Academic research is often interested in complex geological targets, which may lie several kilometers below sea level. At the same time, common acquisition schemes are very likely to suffer from low channel counts and maximum source-receiver offsets that are significantly smaller than the depths of interest. As a consequence, recorded reflections barely exhibit moveout, which lets a majority of common processing steps fail or become unreliable.

[Figure 1 about here.]

While the majority of processing is specifically tailored to reflections or refracted waves, it has been shown in recent works that small-amplitude diffractions possess unique properties, which bear the potential to overcome the aforementioned limitations (e.g. Khaidukov et al. 2004; Fomel et al. 2007; Bauer et al. 2016). Diffraction, just like in optics, where it represents one of the fundamental processes of electromagnetic wave propagation (e.g. Born & Wolf 1980), arguably occurs in any geological subsurface setting and was shown to be a reliable indicator of geodynamically important features like erosional surfaces and, in particular, faults (e.g. Landa & Keydar 1998; Landa et al. 1987; Moser & Howard 2008). In addition, crystalline rocks are known to heavily diffract (Eaton et al. 2003). Owing to their at least partially uniform radiation (Klem-Musatov & Aizenberg 1984), diffracting structures provide superior illumination compared to reflecting interfaces.

Due to their generally low amplitudes, diffracted events are often barely recognizable in seismic sections and mostly masked by more dominant wavefield components, such as direct waves

and in particular reflections (Kozlov et al. 2004). In addition to plane-wave destruction filters (Fomel 2002) and separation based on wavefront attributes (Dell & Gajewski 2011), diffraction imaging in depth has led to results that naturally complement the conventional reflection images and added additional insight (e.g. Moser & Howard 2008; Klovov & Fomel 2012). In this work, we present a simple coherent stacking scheme, that allows for the automatic discrimination between reflected and diffracted contributions by applying filters based on wavefront attributes, which are locally estimated through coherence analysis (see also Dell & Gajewski 2011). While many previous attempts have shown that in the presence of high-amplitude reflections, a clean separation and enhancement of weak diffractions becomes difficult, our suggested workflow specifically targets reflections, which are adapted to the locally coherent wavefield and then subtracted using the aforementioned wavefront filters. For an academic single-channel field data example, acquired near Santorini in the Mediterranean, the coherent subtraction uncovers a surprisingly rich diffracted wavefield that was mostly hidden behind the more dominant reflected events.

2 METHOD

[Figure 2 about here.]

Typically, seismic exploration data is dominated by reflections and the diffracted contributions are hidden and not easily accessible, due to their mostly low amplitudes. To access the diffracted background, we suggest to perform coherence analysis to optimally enhance reflections and then subsequently subtract them from the input data \mathcal{I} . Figure 1 illustrates the individual steps of the presented workflow for a simple synthetic dataset, in which weak diffractions are masked by more dominant coherent reflections.

2.1 Coherent stacking

Stacking is a robust process that is particularly useful, when a coherent signal of interest is of low amplitude and the data is contaminated with random noise (Mayne 1962). In general, the stacked

amplitude \mathcal{S} at a point (\mathbf{x}_0, t_0) of the input data \mathcal{I} can be written as

$$\mathcal{S}(\mathbf{x}_0, t_0) = \sum_i \sum_j \mathcal{I}(\mathbf{x}_i, t_{ij}), \quad (1)$$

where the indices i and j denote lateral trace and time coordinates in the vicinity of the data point, respectively. The lateral trace coordinates \mathbf{x}_i , for 3D acquisitions, are two-dimensional vectors, while the t_{ij} indicate the respective traveltimes to take into account for summation. According to paraxial ray theory (e.g. Schleicher et al. 1993), the traveltimes t_{ij} , in a confined vicinity around the central data point (\mathbf{x}_0, t_0) takes the hyperbolic form

$$t_{ij}^2(\mathbf{x}_i) = (t_{0j} + 2 \mathbf{p} \mathbf{m}_i)^2 + 2 t_{0j} (\mathbf{m}_i^T \mathbf{M} \mathbf{m}_i + \mathbf{h}_i^T \mathbf{H} \mathbf{h}_i), \quad (2)$$

where \mathbf{p} is the two-dimensional horizontal slowness vector and \mathbf{M} and \mathbf{H} correspond to two 2x2 matrices that contain local curvature information on two conceptual wavefronts, one viewed in the zero-offset section, where source and receiver positions coincide, the other in the common-midpoint gather (Hubral 1983). The two-dimensional vectors \mathbf{m}_i and \mathbf{h}_i denote the midpoint displacement and half the source-receiver offset, respectively. Expression (1) together with (2) form the central ingredients of the 3D common-reflection-surface stack (Bergler et al. 2002), which can be automatized by introducing the normalized semblance coefficient (Neidell & Taner 1971) to maximize the local coherence

$$\max_{\mathbf{p}, \mathbf{M}, \mathbf{H}} \frac{1}{n} \frac{\mathcal{S}^2(\mathbf{x}_0, t_0)}{\sum_i \sum_j \mathcal{I}^2(\mathbf{x}_i, t_{ij})}. \quad (3)$$

To make optimal use of data redundancy, both, slope and curvature attributes are estimated simultaneously using a particle swarm optimizer (Kennedy 2011). Through this procedure, emerging wavefronts are characterized for every data sample, which can be utilized for data-driven reflection identification.

2.2 Wavefront filters

As a by-product of the previously described coherence maximization, the locally estimated wavefront attribute fields $(t_0, \mathbf{p}, \mathbf{M}, \mathbf{H})$ can be used for further processing like depth velocity model building using wavefront tomography (Duveneck 2004). Representing the zeroth, first, and second-

order attributes of the emerging wavefronts, these fields can likewise be used to construct filter functions for the distinction between reflections and diffractions. For multi-coverage data, the expression

$$F(\mathbf{M}, \mathbf{H}) = 1 - \exp \left(- \frac{\sum_k \sum_l |M_{kl} - H_{kl}|}{\sum_k \sum_l |M_{kl} + H_{kl}|} \right) \quad (4)$$

compares the local curvatures in the zero-offset data and the common-midpoint gather, which should approach each other for a point-like scatterer (Dell & Gajewski 2011). While originally, the second term in filter function (4) was introduced to suppress reflections rather than diffractions, $F(\mathbf{M}, \mathbf{H})$ now approaches unity for the reflection case and becomes very small for a diffracted wavefront. Since curvatures can only be stably estimated when large apertures are considered, the function

$$F(|\mathbf{p}|) = 1 - \Theta(|\mathbf{p}| - |\mathbf{p}_0|), \quad (5)$$

where Θ is the Heaviside step function, is computationally less demanding. The absolute horizontal slowness $|\mathbf{p}_0|$ represents a user-defined threshold and can be chosen reasonably small, when zero- or near-offset data are considered and reflector dips are moderate, as is commonly the case in sedimentary environments.

As a third alternative, as was recently suggested for passive seismic events, the reference traveltimes t_0 can, like the other wavefront attributes, be treated as a free parameter in the coherence maximization by using $T_{ij} = t_{\text{data}} + t_{ij} - t_0$ instead of t_{ij} as the summation operator (e.g. Schwarz et al. 2016; Khoshnavaz et al. 2017). Just like in equation (4), a comparison of the estimated time t_0 with the actual time coordinate of the data point t_{data} allows for the formulation of the reflection filter

$$F(t_0) = 1 - \exp \left(- \frac{|t_{\text{data}} - t_0|}{|t_{\text{data}} + t_0|} \right), \quad (6)$$

which is applicable in the zero-offset domain. Schwarz et al. (2016) showed that t_0 can only be estimated from traveltimes differences, when the summation operator t_{ij} is hyperbolic (or of higher order), which means that (6) requires even larger data apertures to be sufficiently stable. For the

sake of simplicity, both, the simple illustrative data example (Figure 1) and the academic single-channel field data example (Figures 2, 3) made use of the slope-based filter function (5).

2.3 Coherent subtraction

It is well appreciated that local stacking acts as a directional filter in the data, which is generally undesired, in particular in the context of conventional diffraction separation, since reflections are normally favored (e.g. Hale 1984). Here, we make use of this fact and apply the aforementioned wavefront filter functions together with the directional filtering due to the stacking process to generate reflection-only data \mathcal{R} . The coherent subtraction, just like coherent stacking itself, can be formulated as an optimization problem

$$\min_{\alpha, \tau} \sum_i [\mathcal{I}(\mathbf{x}_i, t_i) - \alpha \mathcal{R}(\mathbf{x}_i, t_i + \tau)]^2, \quad (7)$$

where \mathcal{I} denotes the original unfiltered input data, and t_i is the wavefront-consistent traveltimes at trace i in a vicinity of (\mathbf{x}_0, t_0) . The aperture, i.e. the range of traces investigated in equation (7) should equal the respective choice in the particle swarm optimization of the coherence. The knowledge of the local scaling coefficient α and time correction τ for every data point (\mathbf{x}_0, t_0) then enables the generation of diffraction-only data \mathcal{D} via

$$\mathcal{D}(\mathbf{x}_0, t_0) = \mathcal{I}(\mathbf{x}_0, t_0) - \alpha \mathcal{R}(\mathbf{x}_0, t_0 + \tau). \quad (8)$$

Once again, we perform local coherence analysis using expression (2) together with (3), which leads to pure diffraction attribute sections that, in contrast to reflections, only contain propagation information and, therefore, can directly be used in conventional wavefront tomography (e.g., Bauer et al. 2017). In addition, Schwarz et al. (2016) showed for a 2D example that for diffractions and the near-offset channel only, the wavefront attributes in operator (2) are physically equivalent to the ones arising from a buried passive seismic source excited at the diffractor location. In consequence, the presented workflow of diffractions can likewise be used for passive seismic data.

3 SINGLE-CHANNEL DATA EXAMPLE

[Figure 3 about here.]

In the following, we briefly discuss the results of the application of the suggested coherent subtraction scheme to a 2D line of a single-channel field dataset recorded in the vicinity of the island of Santorini in the Aegean Sea. Exemplary for a typical academic field campaign, the dataset contains signatures related to complicated geological features, including the Kolumbo submarine volcano (Hübscher et al. 2015). Figure 2 shows the diffraction coherence estimated after the subtraction of the dominating reflected contributions using directional stacking and the simple slope-based filter function (5). To illustrate the effectiveness of the proposed automated scheme, Figure 2 includes a comparison of the raw single-channel input data and the respective diffraction coherence achieved for three individual closeups indicated by black frames. While in general, the coherent stacking scheme helped to reveal a surprisingly fine-structured and detailed diffracted background wavefield, the closeups indicate that diffraction occurs largely at every observable unconformity or fault structure.

For further illustration, Figure 3 shows the seismic single-channel section for a small sedimentary basin located at the flank of the submarine volcano (not shown in Figure 2). While the input data (top) is dominated by strong reflections arising from the near-horizontal structures in the sediment body, the image appears reasonably diffuse in the crystalline bedrock. The diffraction coherence (bottom) reveals strong diffractivity in the diffuse hardrock and occasional diffraction related to rugged unconformities and fault systems in the sediment body. This suggests that the normally neglected diffracted wavefield carries information that complements the commonly favored reflection data and adds illumination, e.g. in hardrock environments, which are known to be hard to image conventionally (e.g. Khosnavaz et al. 2016). In correspondence with Figure 1(f)-(h) the presented scheme results in additional data volumes containing the diffracted wavefront's slope and curvature information and the coherence of their focusing, which together with the diffraction-only data can be used for further processing, like, e. g., tomographic model building (Bauer et al. 2017).

4 DISCUSSION

The presented automated scheme makes use of the fact that reflections are normally favored in coherent stacking. Common strategies that involve artificial steering of the summation operator towards fainter contributions often demand large apertures, which may lead to wavelet distortion or leave residual reflected energy in the records. In contrast, the coherent subtraction of a reflection-only stack, generated using simple filter functions that suppress diffracted rather than reflected contributions, is reasonably efficient and leads to a diffraction-only dataset with unaffected amplitudes and unaltered waveforms. Although for common acquisition geometries and relatively shallow targets, reflected energy is most likely to mask diffractions, other wave types such as direct arrivals might likewise be coherently subtracted by supplying alternative wavefront filters. The scheme should also make faint multiple diffractions accessible which might aid more sophisticated processing steps such as diffraction-based interferometry (e.g. Schuster 2016). First tests have revealed that the use of a median instead of a mean filter in the adaptive subtraction can sometimes lead to better results. Despite the fact, that we have restricted ourselves to a 2D academic example, the presented workflow likewise applies to actual 3D data. The diffracted wavefield shown in Figure 2 very likely contains a reasonable amount of out-of-plane energy, due to the superior illumination of diffractions.

Edge diffractions are commonly characterized by a polarity reversal near the apex, which is not accounted for in our formulation of the conventional semblance coefficient (3). However, as long as data apertures are chosen reasonably small, the cancellation of amplitudes during summation is confined to a small vicinity of the edge diffraction's apex. In addition, since we suggest the coherent subtraction of reflections, the separation procedure leaves the polarity unaltered and accessible for further investigations. In the presented data examples, for the sake of simplicity, we used the slope-based wavefront filter (5) to generate the reflection-only data. In the presence of steeply dipping reflections, however, the reliable separation of diffractions can be difficult and we suggest to use a curvature-exploiting filter (e.g. expression (4) or (6)) instead.

The main attraction of the suggested stacking strategy is, that it bears the potential to add usable illumination when source-receiver offsets are short and channel counts are low, as is often the case

in surveys with an academic objective. Diffractions, in contrast to reflections, are not restricted by Snell’s law, which leads to superior illumination of the surrounding medium. Therefore, even for single-channel recordings, they seem ideally suited to investigate anisotropy in the overburden. While using diffractions for imaging itself is not a new concept, most methods are formulated in the depth domain (e.g. Moser & Howard 2008) and require reasonably accurate velocity information, which for academic acquisitions is mostly not available. In contrast, being able to access the diffracted wavefield as it is recorded in the time domain, in turn allows for a *poor man’s* inversion of laterally resolved velocity models using wavefront tomography (Duveneck 2004; Bauer et al. 2017). In addition, conventional single-channel ground-penetrating radar (GPR) as well as 3D high-resolution P-cable data (Planke & Berndt 2007) are expected to equally benefit from the suggested approach.

5 CONCLUSION

We presented a strategy to uncover and use the often neglected diffracted wavefield through coherent subtraction of reflections. While the workflow can be tailored to suppress other dominant wavefield components such as direct arrivals, we suggested several reflection filter functions, useful in different data configurations, based on wavefront attributes which are locally estimated through coherence maximization. Illustrated by a simple synthetic data example, where diffractions were almost entirely masked by more dominant reflections, we showed that the coherent subtraction allowed us to reliably generate and analyze diffraction-only data, even when random noise levels are reasonably high. The application of the coherent subtraction scheme to an academic single-channel field dataset recorded near Santorini in the Aegean Sea revealed a surprisingly rich coherent diffracted wavefield that can be accessed for further processing including efficient laterally resolved depth velocity model building – an option otherwise rarely available in academic environments with low channel counts.

ACKNOWLEDGMENTS

We are grateful to Leon Diekmann, Alexander Bauer, Marcel Ruhna and Jörg Schleicher for important discussions and assistance. In addition, we appreciate the helpful suggestions of Jörg Renner, Ranajit Ghose, and Javad Khosnavaz on how to improve the readability of the paper. The first author is supported by a research fellowship of the German Research Foundation (DFG, SCHW 1870/1-1). This work is also partially supported by the Federal Ministry for Economic Affairs and Energy (BMWi, 03SX427B). We thankfully acknowledge Christian Hübscher for the permission to present the academic field data example from the Mediterranean. The particle swarm optimization was carried out using the Matlab global optimization toolbox and synthetic modeling and visualization was performed with the open-source Seismic Unix software package made available by the Center for Wave Phenomena (CWP) at the Colorado School of Mines.

REFERENCES

- Bauer, A., Schwarz, B., & Gajewski, D., 2016. Enhancement of prestack diffraction data and attributes using a traveltimes decomposition approach, *Studia Geophysica et Geodaetica*, **60**(3), 471–486.
- Bauer, A., Schwarz, B., & Gajewski, D., 2017. Utilizing diffractions in wavefront tomography, *Geophysics*, **80**(2).
- Bergler, S., Hubral, P., Marchetti, P., Cristini, A., & Cardone, G., 2002. 3D common-reflection-surface stack and kinematic wavefield attributes, *The Leading Edge*, **21**(10), 1010–1015.
- Born, M. & Wolf, E., 1980. *Principles of optics: electromagnetic theory of propagation, interference and diffraction of light*, Elsevier.
- Dell, S. & Gajewski, D., 2011. Common-reflection-surface-based workflow for diffraction imaging, *Geophysics*, **76**(5), S187–S195.
- Duveneck, E., 2004. Velocity model estimation with data-derived wavefront attributes, *Geophysics*, **69**(1), 265–274.
- Eaton, D. W., Milkereit, B., & Salisbury, M. H., 2003. *Hardrock seismic exploration*, Society of Exploration Geophysicists.
- Fomel, S., 2002. Applications of plane-wave destruction filters, *Geophysics*, **67**(6), 1946–1960.
- Fomel, S., Landa, E., & Taner, M. T., 2007. Poststack velocity analysis by separation and imaging of seismic diffractions, *Geophysics*, **72**(6), U89–U94.
- Gelius, L.-J. & Tygel, M., 2015. Migration-velocity building in time and depth from 3D (2D) Common-

- Reflection-Surface (CRS) stacking-theoretical framework, *Studia Geophysica et Geodaetica*, **59**(2), 253–282.
- Hale, D., 1984. Dip-moveout by Fourier transform, *Geophysics*, **49**(6), 741–757.
- Hubral, P., 1983. Computing true amplitude reflections in a laterally inhomogeneous earth, *Geophysics*, **48**(8), 1051–1062.
- Hübscher, C., Ruhnau, M., & Nomikou, P., 2015. Volcano-tectonic evolution of the polygenetic Kolumbo submarine volcano/Santorini (Aegean Sea), *Journal of Volcanology and Geothermal Research*, **291**, 101–111.
- Kennedy, J., 2011. Particle swarm optimization, in *Encyclopedia of machine learning*, pp. 760–766, Springer.
- Khaidukov, V., Landa, E., & Moser, T. J., 2004. Diffraction imaging by focusing-defocusing: An outlook on seismic superresolution, *Geophysics*, **69**(6), 1478–1490.
- Khoshnavaz, M. J., Bóna, A., Hossain, M. S., Urosevic, M., & Chambers, K., 2016. Diffraction: Another attribute for the interpretation of seismic data in hard rock environment, a case study, *Interpretation*, **4**(4), B23–B32.
- Khoshnavaz, M. J., Chambers, K., Bóna, A., & Urosevic, M., 2017. Oriented surface passive seismic location using local slopes, *Geophysics*, **82**(2), KS13–KS25.
- Klem-Musatov, K. & Aizenberg, A., 1984. The ray method and the theory of edge waves, *Geophysical Journal International*, **79**(1), 35–50.
- Klokov, A. & Fomel, S., 2012. Separation and imaging of seismic diffractions using migrated dip-angle gathers, *Geophysics*, **77**(6), S131–S143.
- Kozlov, E., Barasky, N., Korolev, E., Antonenko, A., & Koshchuk, E., 2004. Imaging scattering objects masked by specular reflections, in *SEG Technical Program Expanded Abstracts 2004*, pp. 1131–1134, Society of Exploration Geophysicists.
- Landa, E. & Keydar, S., 1998. Seismic monitoring of diffraction images for detection of local heterogeneities, *Geophysics*, **63**(3), 1093–1100.
- Landa, E., Shtivelman, V., & Gelchinsky, B., 1987. A method for detection of diffracted waves on common-offset sections, *Geophysical Prospecting*, **35**(4), 359–373.
- Mayne, W. H., 1962. Common reflection point horizontal data stacking techniques, *Geophysics*, **27**(6), 927–938.
- Moser, T. & Howard, C., 2008. Diffraction imaging in depth, *Geophysical Prospecting*, **56**(5), 627–641.
- Neidell, N. S. & Taner, M. T., 1971. Semblance and other coherency measures for multichannel data, *Geophysics*, **36**(3), 482–497.
- Planke, S. & Berndt, C., 2007. Apparatus for seismic measurements, US Patent 7,221,620.
- Schleicher, J., Tygel, M., & Hubral, P., 1993. Parabolic and hyperbolic paraxial two-point traveltimes in

3D media, *Geophysical Prospecting*, **41**(4), 495–513.

Schuster, G. T., 2016. Seismic interferometry, in *Encyclopedia of Exploration Geophysics*, pp. Q1–1, Society of Exploration Geophysicists.

Schwarz, B., Bauer, A., & Gajewski, D., 2016. Passive seismic source localization via common-reflection-surface attributes, *Studia Geophysica et Geodaetica*, **60**(3), 531–546.

LIST OF FIGURES

- 1 The coherent stacking and subtraction scheme illustrated by a simple synthetic data example. Shown are (a) the diffraction-only data, (b) the actual input data containing strong reflections and noise in addition to the diffractions of (a), (c) the result of the coherent subtraction of the reflection foreground, and (d) the coherent stack of the subtraction result. (e)-(h) display additional by-products, including the local coherence (e), the diffracted wavefront's emergence angle (f), its curvature radius (g), and the coherence of an automated time migration using the aforementioned slope and curvature information (see, e. g., Gelius & Tygel 2015).
- 2 Diffraction coherence of a portion of an academic single-channel field dataset recorded near the island of Santorini in the Aegean Sea. The image (top) corresponds to Figure 1(e) and indicates a very diverse and rich diffracted wavefield that was mostly masked by the reflected contributions and can be attributed to the high geological complexity of the region. The crater of the Kolumbo submarine volcano appears at lateral distances of 13-16 km (Hübscher et al. 2015). Three closeups indicated by the frames are shown before and after the adaptive subtraction of the dominating reflected contributions in the foreground (bottom).
- 3 Seismic single-channel section for a small sedimentary basin at the flank of the Kolumbo submarine volcano (not shown in Figure 2). Noticeably stronger diffractivity can be observed in the crystalline bedrock, whereas in the sediment body, diffraction occurs mainly at the rugged seafloor or is related to an internal unconformity and faulting. While the raw input data (top) is dominated by near-horizontal reflections, the diffraction coherence (bottom) adds complementary structural information.

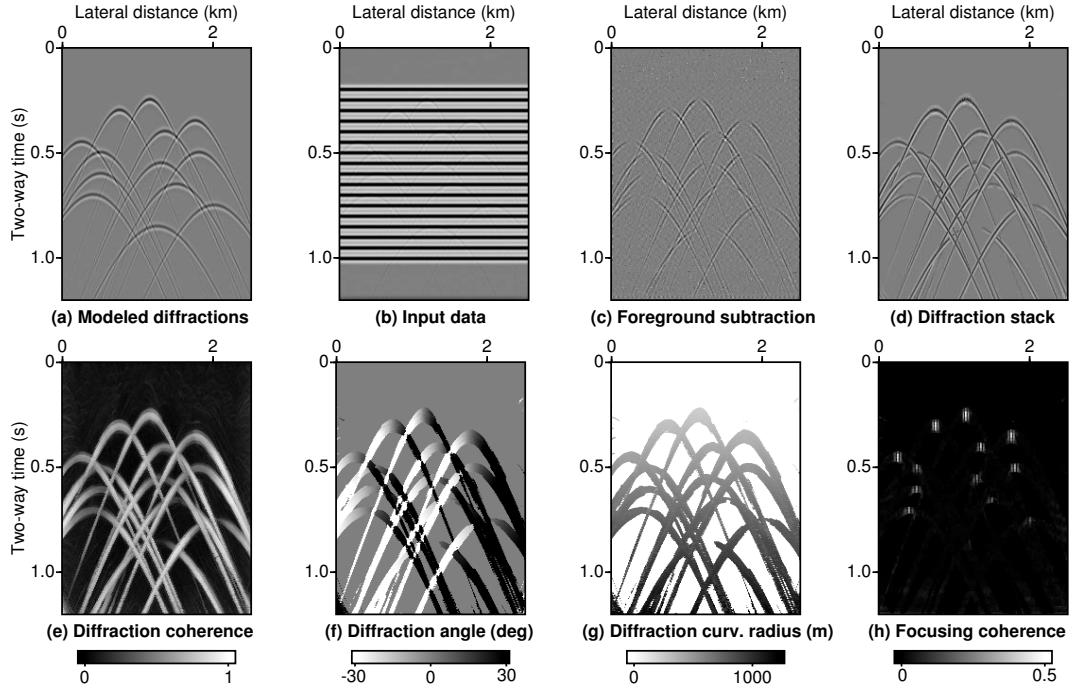


Figure 1. The coherent stacking and subtraction scheme illustrated by a simple synthetic data example. Shown are (a) the diffraction-only data, (b) the actual input data containing strong reflections and noise in addition to the diffractions of (a), (c) the result of the coherent subtraction of the reflection foreground, and (d) the coherent stack of the subtraction result. (e)-(h) display additional by-products, including the local coherence (e), the diffracted wavefront's emergence angle (f), its curvature radius (g), and the coherence of an automated time migration using the aforementioned slope and curvature information (see, e. g., Gelius & Tygel 2015).

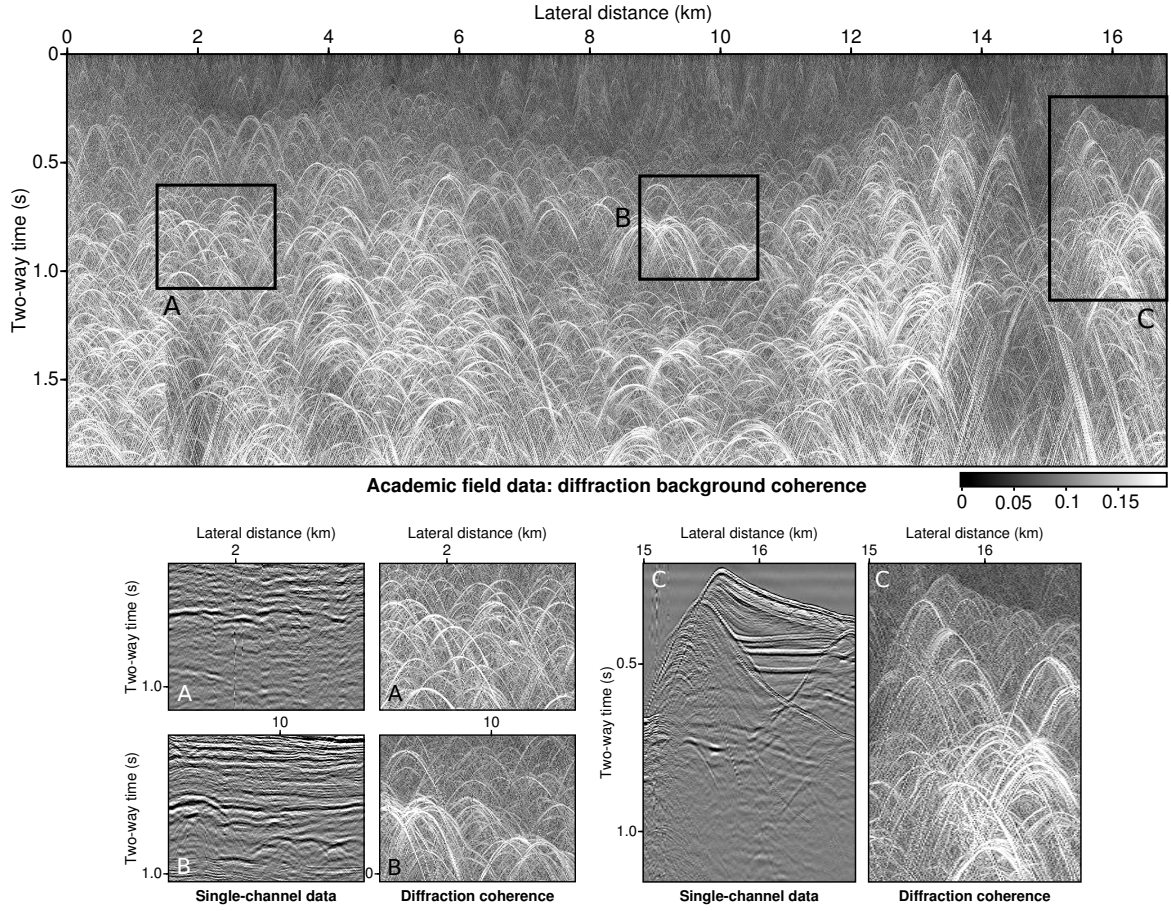


Figure 2. Diffraction coherence of a portion of an academic single-channel field dataset recorded near the island of Santorini in the Aegean Sea. The image (top) corresponds to Figure 1(e) and indicates a very diverse and rich diffracted wavefield that was mostly masked by the reflected contributions and can be attributed to the high geological complexity of the region. The crater of the Kolumbo submarine volcano appears at lateral distances of 13-16 km (Hübscher et al. 2015). Three closeups indicated by the frames are shown before and after the adaptive subtraction of the dominating reflected contributions in the foreground (bottom).

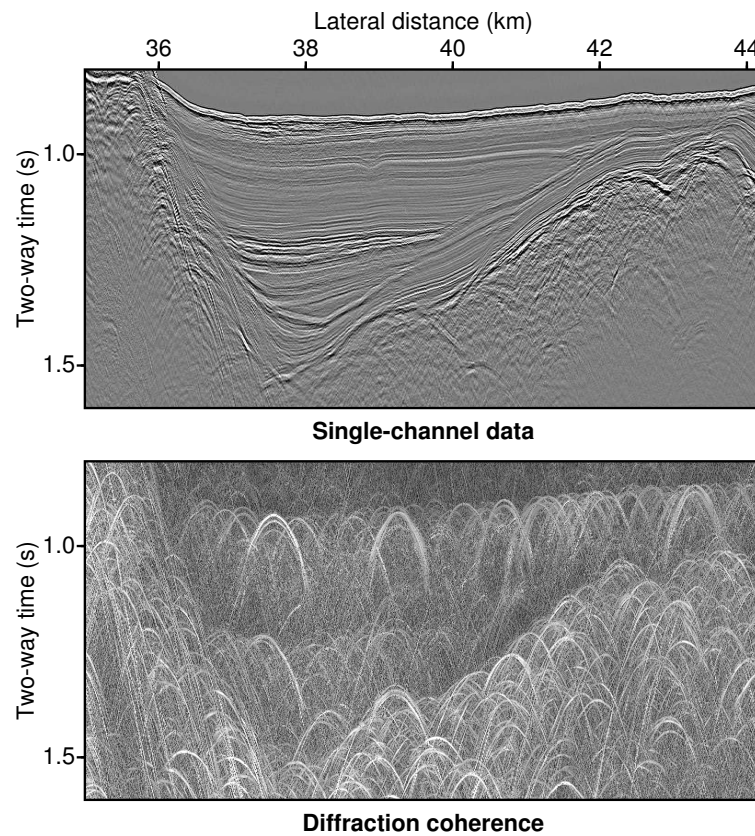


Figure 3. Seismic single-channel section for a small sedimentary basin at the flank of the Kolumbo submarine volcano (not shown in Figure 2). Noticeably stronger diffractivity can be observed in the crystalline bedrock, whereas in the sediment body, diffraction occurs mainly at the rugged seafloor or is related to an internal unconformity and faulting. While the raw input data (top) is dominated by near-horizontal reflections, the diffraction coherence (bottom) adds complementary structural information.